

Berry curvature induced anisotropic magnetotransport in a quadratic triple-component fermionic system

Ojasvi Pal, Bashab Dey and Tarun Kanti Ghosh

Department of Physics, Indian Institute of Technology-Kanpur, Kanpur-208 016, India

Triple-component fermions are pseudospin-1 quasiparticles hosted by certain three-band semimetals in the vicinity of their band-touching nodes [Phys. Rev. B **100**, 235201 (2019)]. The excitations comprise of a flat band and two dispersive bands. The energies of the dispersive bands are $E_{\pm} = \pm \sqrt{\alpha_n^2 k_{\perp}^2 + \nu_z^2 k_z^2}$ with $k_{\perp} = \sqrt{k_x^2 + k_y^2}$ and $n = 1, 2, 3$. In this work, we obtain the exact expression of Berry curvature, approximate form of density of states and Fermi energy as a function of carrier density for any value of n . In particular, we study the Berry curvature induced electrical and thermal magnetotransport properties of quadratic ($n = 2$) triple-component fermions using semiclassical Boltzmann transport formalism. Since the energy spectrum is anisotropic, we consider two orientations of magnetic field (\mathbf{B}): (i) \mathbf{B} applied in the x - y plane and (ii) \mathbf{B} applied in the x - z plane. For both the orientations, the longitudinal and planar magnetoelectric/magnetothermal conductivities show the usual quadratic- B dependence and oscillatory behaviour with respect to the angle between the applied electric field/temperature gradient and magnetic field as observed in other topological semimetals. However, the out-of-plane magnetoconductivity has an oscillatory dependence on angle between the applied fields for the second orientation but is angle-independent for the first one. We observe large differences in the magnitudes of transport coefficients for the two orientations at a given Fermi energy. A noteworthy feature of quadratic triple-component fermions which is typically absent in conventional systems is that certain transport coefficients and their ratios are independent of Fermi energy within the low-energy model.

I. INTRODUCTION

Topologically nontrivial gapless materials termed as topological semimetals have unearthed vast research interests in condensed matter physics within the past few years. Some well-known examples are topological Dirac¹⁻⁵ and Weyl⁶⁻¹³ semimetals which can host emergent quasiparticle excitations analogous to the fermionic elementary particles in high-energy physics. They are characterized by symmetry-protected crossings of two energy bands at the Fermi level. In close vicinity of such band-touching points, the fermionic system can be effectively expressed in terms of pseudospin degrees of freedom, where the distinct eigenvalues of the pseudospin projection corresponds to different energy bands.

Apart from the above mentioned half-integer spin Weyl and Dirac semimetals, recent studies¹⁴ suggested the existence of another class of topological semimetals with three-, six-, or eight-fold degenerate points at the Fermi level that exhibit fermionic quasiparticles having no counterparts in high-energy physics. Furthermore, it was observed that various possible symmetries existing in symmorphic crystals, for instance, mirror and discrete rotational symmetries may lead to topologically protected three-fold degenerate crossing points^{15,16}. It was predicted by first-principles calculations¹⁷⁻²⁰ that several material candidates categorized under symmorphic space groups, such as TaN¹⁸, MoP²¹, WC²², RhSi²³, RhGe²⁴ and ZrTe²⁵ can host crossings of three bands in the neighborhood of the Fermi level. The low energy excitations in such systems behave like pseudospin-1 quasiparticles but obey fermionic statistics and are named as triple-component fermions²⁶ (TCFs). The touching of these

energy bands occurs only in pairs at specific points in the Brillouin zone whose location is decided by the underlying symmetry of the system. Such band-touching points are called triple-component points or nodes.

The general low-energy Hamiltonian of such pseudospin-1 fermionic system in the vicinity of band-touching points can be effectively described as $H = d(\mathbf{k}) \cdot \mathbf{S}$, where $d(\mathbf{k})$ is a function of momenta and \mathbf{S} are the three spin-1 matrices. The low-energy dispersion of the quasiparticle near each node appears as $m\sqrt{\alpha_n^2(k_x^2 + k_y^2)^n + \nu_z^2 k_z^2}$ with $m = \pm 1$ and 0 representing the dispersive and flat bands respectively. Here, the different combination of crystal symmetries²⁷ impose a restriction on n , such that $n \leq 3$. Triple-component fermions are predicted to occur in time-reversal symmetric materials such as Pd₃Bi₂S₂ and Ag₂Se₂Au with space group 199 and 214 respectively¹⁴. The experimental realization of materials having time-reversal symmetry (TRS) broken TCFs is still missing.

The band touching nodes of topological semimetals are sources and drains of Berry curvature^{28,29} which acts as a fictitious magnetic field in the momentum space and leads to several intriguing transport phenomena such as anomalous Hall effect (AHE)²⁹⁻³³, anomalous thermal Hall effect (ATHE)³⁴⁻³⁶, negative longitudinal magnetoresistance (MR)³⁷⁻⁴⁷, planar Hall effect (PHE)⁴⁸⁻⁵² and planar thermal Hall effect (PTHE)⁵³⁻⁵⁵. The Berry curvature induced magnetotransport phenomena in type-I multi-Weyl semimetals has been studied recently⁵⁶. The triple component nodes also give rise to Berry curvature in the two dispersive bands and affect the transport phenomena in presence of magnetic field. Each node hosts a monopole charge of $|2n|$. The magnetotransport

properties²⁶ induced by Berry curvature, ballistic transport across junction⁵⁷ and plasmons⁵⁸ in TRS-broken triple-component fermionic system for $n = 1$ case has been studied recently. In this work, we consider the low-energy model of TRS-broken TCFs specifically for $n = 2$ case (quadratic TCFs) and study its Berry curvature induced electrical and thermal magnetotransport properties. The dispersion of quadratic TCFs has different scaling with momenta along different directions which allows us to use two orientations of planar Hall geometry to develop our understanding towards the behavior of magnetotransport coefficients in response to linear dispersion along one symmetry direction and quadratic dispersion for the other two directions. Hence measurement of transport coefficients in presence of small magnetic field may act as a probe for detecting different symmetry axes of the system.

This paper is organized as follows: In Sec. II, we present a discussion on the low-energy model for generalized triple component fermions. In Sec. III, we provide a review of the semiclassical Boltzmann transport formalism incorporating the Berry curvature effects. In Sec. IV, we obtain the expressions of magnetoconductivities in the presence of in-plane electric and magnetic fields and further discuss the magnetic field and angular dependence of our numerically computed results of longitudinal magnetoconductivity (LMC) and planar Hall conductivity (PHC) for two different orientations of electric and magnetic fields. Section V is dedicated to the detailed discussion of magnetoresistance. The results of positive longitudinal magneto-thermal conductivity (LMTC) and planar thermal Hall conductivity (PTHC) are presented in Sec. VI. In Sec. VII, we make a quantitative comparison of the transport coefficients calculated for the two configurations. Finally, we summarize our main results in Sec. VIII.

II. LOW-ENERGY MODEL FOR GENERALIZED TRIPLE COMPONENT FERMIONS

The effective low-energy Hamiltonian for TRS broken generalized TCFs can be expressed as²⁶

$$H_{n,\tau}(\mathbf{k}) = d_1^n(\mathbf{k})S_x + d_2^n(\mathbf{k})S_y + \tau d_3(\mathbf{k})S_z, \quad (1)$$

where $\tau = \pm 1$ is the valley index representing the two valleys or triple-component points and S_x , S_y , and S_z are the components of spin-1 matrix operator given by

$$S_x = \frac{1}{\sqrt{2}} \begin{pmatrix} 0 & 1 & 0 \\ 1 & 0 & 1 \\ 0 & 1 & 0 \end{pmatrix}, \quad S_y = \frac{1}{\sqrt{2}} \begin{pmatrix} 0 & -i & 0 \\ i & 0 & -i \\ 0 & i & 0 \end{pmatrix}, \quad (2)$$

$$S_z = \begin{pmatrix} 1 & 0 & 0 \\ 0 & 0 & 0 \\ 0 & 0 & -1 \end{pmatrix}.$$

Here, the different combinations of symmetries in pseudospin-1 fermionic systems impose a restriction on

n , i.e., $n \leq 3$. The coefficients $d_{1,2,3}^n(\mathbf{k})$ are functions of momenta which vary according to the given choice of n ²⁶. The Hamiltonian in Eq.(1) can be rewritten compactly as

$$H_{n,\tau}(\mathbf{k}) = \alpha_n k_\perp^n (S_x \cos n\phi + S_y \sin n\phi) + \tau \nu_z k_z S_z, \quad (3)$$

where $k_\perp = \sqrt{k_x^2 + k_y^2}$, ν_z/\hbar and α_1/\hbar have the dimension of velocity, α_2/\hbar^2 has the dimension of inverse mass and α_3 has the dimension of inverse of density of states. The diagonalization of the Hamiltonian leads to the energy spectra in the neighborhood of each valley as

$$\epsilon_n^m(\mathbf{k}) = m \sqrt{\alpha_n^2 k_\perp^{2n} + \nu_z^2 k_z^2}, \quad (4)$$

where $m = -1, 0, 1$ is the pseudospin projection. The dispersive bands with $m = \pm 1$ indicate the conduction and valence bands respectively and $m = 0$ represents the flat band at zero energy. For $n = 1$, the two dispersive bands scale linearly with all the three components of momentum. These excitations are called linear TCFs. For $n = 2$, the excitations are named as quadratic TCFs since the energy scales linearly with k_z but quadratically with k_\perp . Cubic TCFs refer to the $n = 3$ case, where the energy scales linearly with k_z but cubically with k_\perp .

The eigenstates corresponding to the three bands can be written as

$$|\psi_{n,\tau,\mathbf{k}}^+\rangle = \begin{pmatrix} \left(\frac{1+\tau \cos \gamma_n}{2}\right) \\ \frac{\sin \gamma_n}{\sqrt{2}} e^{in\phi} \\ \left(\frac{1-\tau \cos \gamma_n}{2}\right) e^{2in\phi} \end{pmatrix}, \quad (5)$$

$$|\psi_{n,\tau,\mathbf{k}}^-\rangle = \begin{pmatrix} \left(\frac{1-\tau \cos \gamma_n}{2}\right) \\ -\frac{\sin \gamma_n}{\sqrt{2}} e^{in\phi} \\ \left(\frac{1+\tau \cos \gamma_n}{2}\right) e^{2in\phi} \end{pmatrix}, \quad (6)$$

and

$$|\psi_{n,\tau,\mathbf{k}}^0\rangle = \begin{pmatrix} -\frac{\sin \gamma_n}{\sqrt{2}} \\ \tau \cos \gamma_n e^{in\phi} \\ \frac{\sin \gamma_n}{\sqrt{2}} e^{2in\phi} \end{pmatrix}. \quad (7)$$

Here, we define $\gamma_n = \tan^{-1}[(\alpha_n/\nu_z) \tan \theta (k \sin \theta)^{n-1}]$. The expectation value of components of the spin-1 matrix operator with respect to the eigenstates $|\psi_{n,\tau,\mathbf{k}}^m\rangle$ are calculated as: $\langle S_x \rangle_m = m(\sin \gamma_n) \cos n\phi$, $\langle S_y \rangle_m = m(\sin \gamma_n) \sin n\phi$ and $\langle S_z \rangle_m = m \cos \gamma_n$.

The touching points of non-degenerate pair of bands in the momentum space act as a source and sink of the Abelian Berry curvature. The Berry curvature of the m th band for the Hamiltonian given by Eq. (3) can be calculated using $\Omega_{n,\tau,\mathbf{k}}^m = i \nabla_{\mathbf{k}} \times \langle \psi_{n,\tau,\mathbf{k}}^m | \nabla_{\mathbf{k}} | \psi_{n,\tau,\mathbf{k}}^m \rangle$ as²⁹

$$\mathbf{\Omega}_{n,\tau,\mathbf{k}}^m = mn\tau\nu_z\alpha_n^2 k^{(2n-4)} \left[\frac{-(\sin\theta)^{2n-2} [1 + (n-1)\cos^2\theta]\hat{k} + [(n-1)\cos\theta(\sin\theta)^{2n-1}]\hat{\theta}}{(\alpha_n^2 k^{2n-2}(\sin\theta)^{2n} + \nu_z^2 \cos^2\theta)^{3/2}} \right]. \quad (8)$$

The Berry curvature of the flat band is identically zero for all momenta, but is finite for the two dispersive bands carrying opposite signs. The Berry curvature of linear TCFs contains only the radial component while that of quadratic and cubic TCFs have angular components apart from the radial ones. In the k_x - k_y plane, the Berry curvature varies as $\sim mn\tau\nu_z/(\alpha_n k^{n+1})\hat{k}$. Integrating the Berry curvature over a unit sphere enclosing the triple-component point defines the monopole charge, given by

$$\aleph = \frac{1}{2\pi} \int_A \mathbf{\Omega}_{\mathbf{k}} \cdot d\mathbf{A} = 2n. \quad (9)$$

The vector plots of Berry curvature of conduction band for TCFs with $n = 1, 2, 3$ and $\tau = 1$ in k_x - k_y plane and k_x - k_z plane are shown in Fig. 1. The angular dependence of Berry curvature for $n = 2$ and $n = 3$ can be seen in the plots for k_x - k_z plane. The converging nature of arrows represents the sink of Berry curvature at the origin.

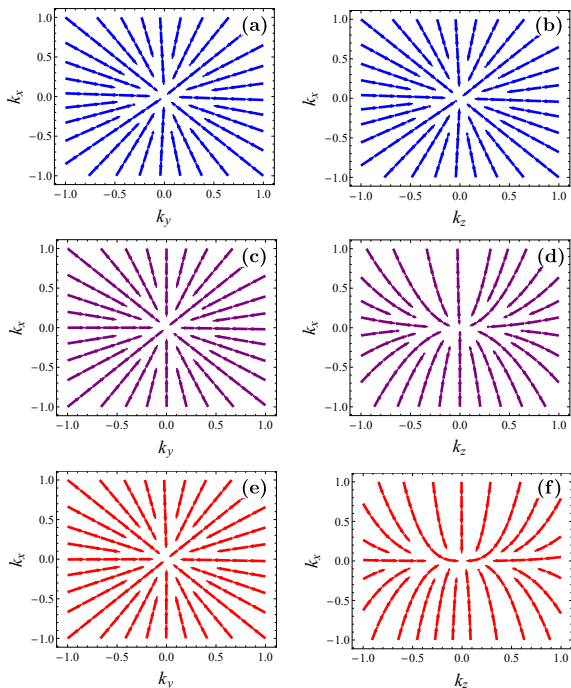


FIG. 1: Vector plots of the Berry curvature of the conduction band for triple-component semimetals – upper row: $n = 1$, middle row: $n = 2$ and lower row: $n = 3$ in k_x - k_y plane and k_x - k_z plane respectively.

The density of states (DOS) for linear TCFs including

valley degeneracy is given by

$$D_1(\mu) = D'_1 \frac{\tilde{\mu}^2}{2\pi^2}, \quad (10)$$

where $D'_1 = 2k'^2\nu_z/\alpha_1^2$ and $\tilde{\mu} = \mu/\mu'_1$ with $\mu'_1 = k'\nu_z$ being an energy scale and k' an arbitrary wavenumber scale. The DOS for quadratic TCFs can be obtained as

$$D_2(\mu) = D'_2 \int_0^\pi d\theta \left(\frac{\tilde{\mu} \sqrt{-\cos^2\theta + \sqrt{\cos^4\theta + 4\tilde{\mu}^2 \sin^4\theta}}}{4\sqrt{2}\pi^2 \sin\theta \sqrt{\cos^4\theta + 4\tilde{\mu}^2 \sin^4\theta}} \right) \quad (11)$$

Here, we have defined $D'_2 = 2\nu_z/\alpha_2^2$ and $\tilde{\mu} = \mu/\mu'_2$ with

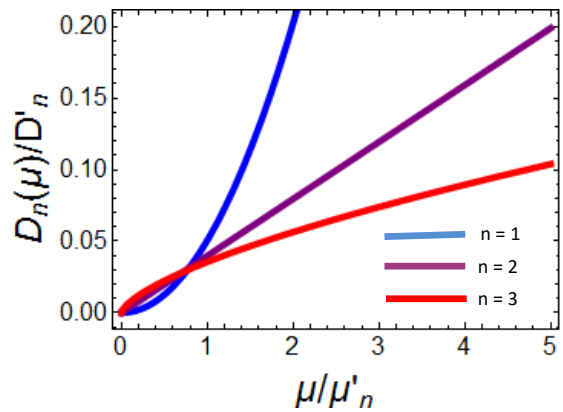


FIG. 2: Density of states as a function of the Fermi energy for triple-component semimetals with $n = 1, 2, 3$.

$\mu'_2 = \nu_z^2/\alpha_2$. Unlike Weyl semimetals and 3D free electron gas, the variation of DOS in quadratic TCFs is approximately linear in energy. For cubic TCFs, the integral expression of DOS is cumbersome and hence not presented here. We numerically find that $D_3(\mu)/D'_3$ varies approximately as $\tilde{\mu}^{2/3}$, where $D'_3 = 2/\alpha_3$ and $\tilde{\mu} = \mu/\mu'_3$ with $\mu'_3 = \nu_z^{3/2}/\alpha_3^{1/2}$. Hence, the DOS of generalized TCFs varies with Fermi energy as $D_n(\mu) \sim \mu^{2/n}$, where $n = 1, 2, 3$, as shown in Fig. 2. The electron density n_e at temperature T can be obtained from the following condition,

$$n_e = \int_0^\infty f_{eq}(\mu) D(\mu) d\mu \quad (12)$$

where $f_{eq}(\mu)$ is equilibrium Fermi-Dirac distribution function. In linear TCFs, the Fermi energy varies with electron density at $T \rightarrow 0$ as $\mu/\mu'_1 \sim (n_e/n'_1)^{1/3}$ with

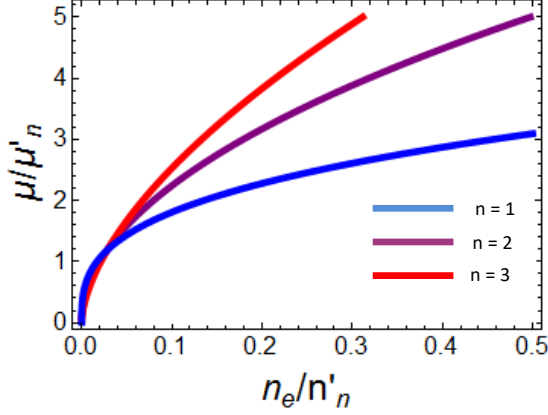


FIG. 3: Plots of variation of the Fermi energy with electron density in the $T \rightarrow 0$ limit for linear, quadratic and cubic TCFs.

$n'_1 = k'^3 \nu_z^2 / \alpha_1^2$. The quadratic and cubic TCFs show the variation with electron density as $\mu/\mu'_2 \sim (n_e/n'_2)^{1/2}$ and $\mu/\mu'_3 \sim (n_e/n'_3)^{3/5}$ with $n'_2 = (\nu_z/\alpha_2)^3$ and $n'_3 = (\nu_z/\alpha_3)^{3/2}$ respectively. In Fig. 3, we have plotted the Fermi energy as a function of electron density for generalized TCFs which scales as $\mu \sim (n_e)^{\frac{n}{n+2}}$.

III. THEORETICAL FORMULATION

We will use Boltzmann transport formalism to obtain the magnetotransport properties of quadratic TCFs. The semiclassical Boltzmann transport approach is valid for weak magnetic fields such that $\omega_c \tau \ll 1$, where ω_c is the cyclotron frequency and τ is the average time between two successive collisions. In this limit, the Landau quantization gets wiped out by disorder effects.

The phenomenological Boltzmann transport equation (BTE) for the non-equilibrium distribution function $f_{\mathbf{r},\mathbf{k},t}^m$ is given by⁵⁹

$$\left(\frac{\partial}{\partial t} + \dot{\mathbf{r}}^m \cdot \nabla_{\mathbf{r}} + \dot{\mathbf{k}}^m \cdot \nabla_{\mathbf{k}} \right) f_{\mathbf{r},\mathbf{k},t}^m = I_{\text{coll}}\{f_{\mathbf{r},\mathbf{k},t}^m\}, \quad (13)$$

where right-hand side represents the collision integral and m is the band index. Under the relaxation-time approximation, the collision integral takes the form, $I_{\text{coll}}\{f_{\mathbf{k}}^m\} = -\frac{f_{\mathbf{k}}^m - f_{\text{eq}}^m}{\tau_{\mathbf{k}}^m}$, where the scattering time scale $\tau_{\mathbf{k}}^m$ is the intranode relaxation time and $f_{\text{eq}}^m = [1 + e^{\beta(\epsilon_{\mathbf{k}}^m - \mu)}]^{-1}$ is the equilibrium Fermi-Dirac distribution function. We will ignore the momentum dependence of relaxation time and assumed it to be constant throughout the paper. In the steady-state condition, the BTE takes the following form

$$(\dot{\mathbf{r}}^m \cdot \nabla_{\mathbf{r}} + \dot{\mathbf{k}}^m \cdot \nabla_{\mathbf{k}}) f_{\mathbf{k}}^m = -\frac{f_{\mathbf{k}}^m - f_{\text{eq}}^m}{\tau}. \quad (14)$$

The modified semiclassical equations of motion for an electron incorporating the Berry curvature effects are given by^{29,60,61}

$$\dot{\mathbf{r}}^m = \frac{1}{D_{\mathbf{k}}^m} \left[\mathbf{v}_{\mathbf{k}}^m + \frac{e}{\hbar} (\mathbf{E} \times \boldsymbol{\Omega}_{\mathbf{k}}^m) + \frac{e}{\hbar} (\mathbf{v}_{\mathbf{k}}^m \cdot \boldsymbol{\Omega}_{\mathbf{k}}^m) \mathbf{B} \right], \quad (15)$$

$$\hbar \dot{\mathbf{k}}^m = \frac{1}{D_{\mathbf{k}}^m} \left[-e\mathbf{E} - e(\mathbf{v}_{\mathbf{k}}^m \times \mathbf{B}) - \frac{e^2}{\hbar} (\mathbf{E} \cdot \mathbf{B}) \boldsymbol{\Omega}_{\mathbf{k}}^m \right], \quad (16)$$

where $D_{\mathbf{k}}^m = (1 + \frac{e\mathbf{B} \cdot \boldsymbol{\Omega}_{\mathbf{k}}^m}{\hbar})$ is the phase space factor which alters the invariant phase space volume for Berry curvature modified dynamics as $[d\mathbf{k}] = D_{\mathbf{k}}^{-1} [d\mathbf{k}]$ ⁶², where $[d\mathbf{k}] = d^3k/(2\pi)^3$. To balance this changed phase space volume, the density of states is multiplied by $D_{\mathbf{k}}$, so that the number of states in the volume element remains unchanged.

Here, the second term of Eq. (15) is the anomalous Hall velocity^{29–32} arising due to Berry curvature and the third term $(\mathbf{v}_{\mathbf{k}}^m \cdot \boldsymbol{\Omega}_{\mathbf{k}}^m) \mathbf{B}$ give rise to the chiral magnetic effect^{63,64}. In Eq. (16), the first two terms describes the Lorentz force whereas the last term is responsible for chiral anomaly effect^{64–67}.

Substituting Eqs. (15) and (16) in Eq. (14), we obtained the following expression of non-equilibrium distribution function defined upto linear order in \mathbf{E} and ∇T as

$$f_{\mathbf{k}}^m = f_{\text{eq}}^m + \left[\frac{\tau}{D_{\mathbf{k}}^m} \left(-e\mathbf{E} - \frac{(\epsilon_{\mathbf{k}}^m - \mu)}{T} \nabla T \right) \cdot \left(\mathbf{v}_{\mathbf{k}}^m + \frac{e}{\hbar} \mathbf{B} (\mathbf{v}_{\mathbf{k}}^m \cdot \boldsymbol{\Omega}_{\mathbf{k}}^m) + \mathbf{v}_{\mathbf{k}}^m \cdot \boldsymbol{\Gamma}_{\mathbf{k}}^m \right) \right] \left(-\frac{\partial f_{\text{eq}}^m}{\partial \epsilon_{\mathbf{k}}^m} \right). \quad (17)$$

The second term in the above expression denotes the deviation from equilibrium. The term $(\mathbf{v}_{\mathbf{k}}^m \cdot \boldsymbol{\Gamma}_{\mathbf{k}}^m)$ represents the Lorentz force contribution whose analytical expressions are given in the Appendix A^{48,55}. Since the prime focus of this paper is to study the effect of Berry curvature in transport coefficients, we have not considered the Lorentz force contribution to the conductivity. The linear response equations for the charge current (\mathbf{j}^e) and thermal current (\mathbf{j}^q) to the external fields can be written as⁵⁹

$$\mathbf{j}_a^e = L_{ab}^{11} E_b + L_{ab}^{12} (-\nabla_b T), \quad (18)$$

and

$$\mathbf{j}_a^q = L_{ab}^{21} E_b + L_{ab}^{22} (-\nabla_b T), \quad (19)$$

where a and b are the spatial indices running over x , y and z . The set of L represents the transport coefficients, for instance, L^{11} and L^{22} are the electrical and thermal conductivities respectively. The thermopower is defined as $S = L^{12}/L^{11}$. The Onsager's relation relates the L^{12} and L^{21} as $L^{21} = TL^{12}$.

In the subsequent sections, we study the Berry curvature driven Boltzmann transport phenomena for quadratic TCFs.

IV. ELECTRICAL TRANSPORT

In the absence of thermal gradient, the charge current is defined as

$$\mathbf{j} = -e \sum_m \int [d\mathbf{k}] D_{\mathbf{k}}^m(\mathbf{r}^m) f_{\mathbf{k}}^m, \quad (20)$$

Substituting Eqs. (15) and (17) in Eq. (20), we obtain the general expression of Berry curvature dependent electric conductivity as:

$$\begin{aligned} \sigma_{ij} = & -\frac{e^2}{\hbar} \sum_m \int [d\mathbf{k}] \epsilon_{ijl} (\Omega_{\mathbf{k}}^{m,l}) f_{\text{eq}}^m \\ & + e^2 \tau \sum_m \int [d\mathbf{k}] (D_{\mathbf{k}}^m)^{-1} \left(v_i^m + \frac{e}{\hbar} B_i (\mathbf{v}_{\mathbf{k}}^m \cdot \boldsymbol{\Omega}_{\mathbf{k}}^m) \right) \\ & \left(v_j^m + \frac{e}{\hbar} B_j (\mathbf{v}_{\mathbf{k}}^m \cdot \boldsymbol{\Omega}_{\mathbf{k}}^m) \right) \left(-\frac{\partial f_{\text{eq}}^m}{\partial \epsilon_{\mathbf{k}}^m} \right), \end{aligned} \quad (21)$$

where ϵ_{ijl} is the Levi-Civita tensor and $\Omega_{\mathbf{k}}^{m,l}$ denotes the l -component of Berry curvature. We expand the term $(D_{\mathbf{k}}^m)^{-1}$ upto quadratic order in \mathbf{B} -field as $(1 + (e/\hbar)\mathbf{B} \cdot \boldsymbol{\Omega}_{\mathbf{k}}^m)^{-1} = 1 - (e/\hbar)\mathbf{B} \cdot \boldsymbol{\Omega}_{\mathbf{k}}^m + (e^2/\hbar^2)(\mathbf{B} \cdot \boldsymbol{\Omega}_{\mathbf{k}}^m)^2$ in order to express the conductivity in power of magnetic field by separating various B -contributions. For the above expansion to converge, we must have $(\frac{eB\Omega_z}{\hbar}) \ll 1$. We find that the above condition is satisfied when $\tilde{\mu} \gg 3.5$ for $\tilde{B} = 2$, where $\tilde{B} = B/B_0$ and $\tilde{\mu} = \mu/\mu_0$ with $B_0 = \nu_z^2 \hbar / e\alpha_2^2$ and $\mu_0 = \nu_z^2 / \alpha_2$ being the magnetic field and energy scales respectively, of the given system. Therefore, for the rest of our calculations, we choose $\tilde{B} = 2$ and $\tilde{\mu} = 10$.

We emphasize that out of three bands, only the two dispersive bands participate in the transport properties. In this work, we choose $\mu > 0$ and thus Eq. (21) will have contribution only from conduction band ($m = 1$). Therefore, we drop the band index m for rest of the paper to investigate these quantities. The first term of Eq. (21) represents the Berry curvature induced intrinsic anomalous Hall conductivity. Since we are interested in calculation of transport coefficients in presence of magnetic field, we neglect the anomalous term.

It is to be noted that the magnetotransport results will be qualitatively same for both low-energy model and lattice model as long as Fermi energy is close to the nodes. However, the calculation of anomalous Hall conductivity using low-energy model gives completely different result as that obtained from the tight-binding model. In low-energy model, anomalous Hall conductivity trivially vanishes, whereas for lattice model it is finite and proportional to the distance between the nodes²⁶.

Drude conductivities

In the absence of magnetic field, the diagonal components of conductivity matrix are called Drude conductivity ($\sigma_{ii}^{(0)}$). We compute the Drude conductivities of quadratic TCFs in this section and discuss their dependence on Fermi energy. In the wake of anisotropic energy spectrum of quadratic TCFs, we have $\sigma_{xx}^{(0)} = \sigma_{yy}^{(0)} \neq \sigma_{zz}^{(0)}$. The general form of Drude conductivity is given by

$$\sigma_{ii}^{(0)} = e^2 \tau \int \frac{d^3 k}{(2\pi)^3} v_i^2 \left(-\frac{\partial f_{\text{eq}}}{\partial \epsilon_{\mathbf{k}}} \right), \quad (22)$$

where we know that $(-\partial f_{\text{eq}}/\partial \epsilon_{\mathbf{k}}) = \delta(\mu - \epsilon_{\mathbf{k}})$ in the zero temperature limit. The semiclassical band velocities of the system can be obtained as

$$v_x = \frac{2\alpha_2^2 k^2 \sin^3 \theta \cos \phi}{\hbar \sqrt{\alpha_2^2 k^2 \sin^4 \theta + \nu_z^2 \cos^2 \theta}}, \quad (23)$$

$$v_y = \frac{2\alpha_2^2 k^2 \sin^3 \theta \sin \phi}{\hbar \sqrt{\alpha_2^2 k^2 \sin^4 \theta + \nu_z^2 \cos^2 \theta}}, \quad (24)$$

and

$$v_z = \frac{\nu_z^2 \cos \theta}{\hbar \sqrt{\alpha_2^2 k^2 \sin^4 \theta + \nu_z^2 \cos^2 \theta}}. \quad (25)$$

The Drude conductivity along the x direction can be obtained as:

$$\sigma_{xx}^{(0)} = \frac{e^2 \tau}{(2\pi)^3} \int_0^\pi \sin \theta d\theta \int_0^{2\pi} d\phi \int_0^\infty k^2 dk v_x^2 \delta(\mu - \epsilon_{\mathbf{k}}). \quad (26)$$

We have used the property of Dirac delta function to evaluate the above integrand which is given by

$$\delta[g(x)] = \sum_i \frac{\delta(x - x_i)}{|g'(x_i)|}, \quad (27)$$

where x_i are the roots or zeroes of function $g(x)$. For the case of quadratic TCFs, using the above equation, $\delta(\mu - \epsilon_{\mathbf{k}}) \equiv \delta[g(k)]$ can be written as

$$\delta \left[\mu - \sqrt{\alpha_2^2 k^4 \sin^4 \theta + \nu_z^2 k^2 \cos^2 \theta} \right] = \frac{\delta(k - k_F)}{|g'(k_F)|}, \quad (28)$$

where the root of $g(k)$ for the conduction band is obtained as

$$k_F = \left(\frac{-\nu_z^2 \cos^2 \theta + \sqrt{\nu_z^4 \cos^4 \theta + 4\alpha_2^2 \mu^2 \sin^4 \theta}}{2\alpha_2^2 \sin^4 \theta} \right)^{1/2}. \quad (29)$$

Using the expression of k_F in eq. (26), we get

$$\sigma_{xx}^{(0)} = 2 \left(\frac{e^2 \tau \nu_z^3}{8\sqrt{2}\pi^2 \alpha_2^2 \hbar^2} \right) \int_0^\pi d\theta \left(\frac{\left(-\cos^2 \theta + \sqrt{\cos^4 \theta + 4\tilde{\mu}^2 \sin^4 \theta} \right)^3}{\sin^5 \theta \left(\sqrt{\cos^4 \theta + 4\tilde{\mu}^2 \sin^4 \theta} \right) \left(\sqrt{\cos^2 \theta + \sqrt{\cos^4 \theta + 4\tilde{\mu}^2 \sin^4 \theta}} \right)} \right) \quad (30)$$

and $\sigma_{yy}^{(0)} = \sigma_{xx}^{(0)}$. The Drude conductivity along the z direction is obtained as

$$\sigma_{zz}^{(0)} = 2 \left(\frac{e^2 \tau \nu_z^3}{8\sqrt{2}\pi^2 \alpha_2^2 \hbar^2} \right) \int_0^\pi d\theta \left(\frac{-\cos^2 \theta + \sqrt{\cos^4 \theta + 4\tilde{\mu}^2 \sin^4 \theta}}{\sin^3 \theta \sqrt{\cos^4 \theta + 4\tilde{\mu}^2 \sin^4 \theta}} \right) \left(\frac{2 \cos^2 \theta}{\sqrt{\cos^2 \theta + \sqrt{\cos^4 \theta + 4\tilde{\mu}^2 \sin^4 \theta}}} \right). \quad (31)$$

In the above expressions, an overall factor of 2 is multiplied, covering the contributions from two triple-component nodes. We have plotted the numerically calculated Drude conductivities as a function of the Fermi energy in Fig. 4(a) and 4(b). The large difference in the values of $\sigma_{xx}^{(0)}$ and $\sigma_{zz}^{(0)}$ illustrates the strong anisotropic nature of the system. The variation of $\sigma_{zz}^{(0)}$ is more linear in Fermi energy than $\sigma_{xx}^{(0)}$. Next, we consider the

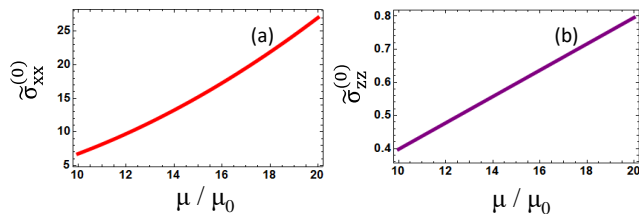


FIG. 4: (a)-(b) The variation of Drude conductivities with the Fermi energy for the quadratic TCFs, $\sigma_{xx}^{(0)}$ shows more increase with the Fermi energy as compared to $\sigma_{zz}^{(0)}$. We have defined $\tilde{\sigma} = \sigma/\sigma_0$ with $\sigma_0 = \tau e^2 \nu_z^3 / \hbar^2 \alpha_2^2$.

two orientations of magnetic field i.e., \mathbf{B} in the x - y plane and \mathbf{B} in the x - z plane. We have computed numerically the different components of electrical conductivity for the low-energy model of the quadratic TCFs (including the contribution of two triple-component nodes) in the following subsections.

A. Magnetic field applied in the x - y plane

We consider a planar Hall geometry where the applied electric field is along the x axis ($\mathbf{E} = E\hat{x}$) and the magnetic field is confined in the x - y plane making an angle β with the x axis, i.e., $\mathbf{B} = (B \cos \beta, B \sin \beta, 0)$ as shown in Fig. 5(a). The electric and magnetic fields are parallel to each other at $\beta = 0$ resulting in maximum value of $\mathbf{E} \cdot \mathbf{B}$.

The expression for the longitudinal magnetoconductivity using Eq. (21) can be written as

$$\sigma_{xx} = e^2 \tau \int \frac{d^3 k}{(2\pi)^3} D_{\mathbf{k}}^{-1} \left[v_x + \frac{eB \cos \beta}{\hbar} (\mathbf{v}_{\mathbf{k}} \cdot \boldsymbol{\Omega}_{\mathbf{k}}) \right]^2 \left(-\frac{\partial f_{\text{eq}}}{\partial \epsilon_{\mathbf{k}}} \right), \quad (32)$$

Further, the magnetoconductivity in the planar configuration σ_{xx} can be expressed explicitly in terms of σ_{\parallel} and σ_{\perp} as

$$\sigma_{xx} = \sigma_{\perp} + \Delta \sigma \cos^2 \beta, \quad (33)$$

where $\Delta \sigma = \sigma_{\parallel} - \sigma_{\perp}$ with $\sigma_{\parallel} = \sigma_{xx}(\beta = 0) = \sigma_{xx}^{(0)} + \sigma_{\parallel}^{(2)}$ and $\sigma_{\perp} = \sigma_{xx}(\beta = \pi/2) = \sigma_{xx}^{(0)} + \sigma_{\perp}^{(2)}$. The $\cos^2 \beta$ results in oscillations in the longitudinal magnetoconductivity when the magnetic field is rotated in the x - y plane, as shown in Fig. 5(b). The B^2 dependence of LMC is depicted in Fig. 5(c) for $\beta = 0$.

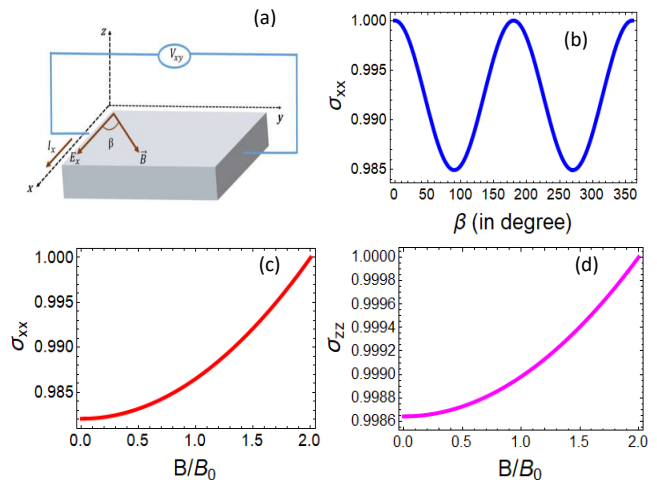


FIG. 5: (a) Schematic illustration of the planar Hall effect geometry. The electric field (\mathbf{E}) is applied along the x -axis and the magnetic field (\mathbf{B}) is applied in the x - y plane at an angle β from the x -axis. The V_{xy} is measured as an in-plane induced voltage perpendicular to the direction of the electric field. (b) The angular dependence of longitudinal magnetoconductivity ($\sigma_{xx} \propto \cos^2 \beta$) computed numerically from the low-energy model of the quadratic TCFs at $B/B_0 = 2$, where the y axis is normalized by $\sigma_{xx}(\beta = 0)$. (c) and (d) depicts the variation of LMC at $\beta = 0$ (normalized by σ_{xx} for $B/B_0 = 2$) and the out-of-plane magnetoconductivity σ_{zz} (normalized by σ_{zz} for $B/B_0 = 2$) as a function of magnetic field and their amplitude in both the cases shows B^2 dependence respectively. Here, we have used the parameter: $\mu/\mu_0 = 10$.

Planar Hall effect: We observe planar Hall effect (PHE) in the quadratic TCFs for the given planar geometry. The PHE^{48,49} refers to a phenomenon where a voltage is induced perpendicular to the applied electric field in presence of a magnetic field which is coplanar with the applied field and the induced voltage. The expression for planar Hall conductivity (PHC) is obtained as

$$\sigma_{yx} = e^2\tau \int \frac{d^3k}{(2\pi)^3} (D_{\mathbf{k}})^{-1} \left[v_x + \frac{eB \cos \beta}{\hbar} (\mathbf{v}_{\mathbf{k}} \cdot \boldsymbol{\Omega}_{\mathbf{k}}) \right] \left[v_y + \frac{eB \sin \beta}{\hbar} (\mathbf{v}_{\mathbf{k}} \cdot \boldsymbol{\Omega}_{\mathbf{k}}) \right] \left(-\frac{\partial f_{\text{eq}}}{\partial \epsilon_{\mathbf{k}}} \right), \quad (34)$$

Using the above expression, the PHC can be written as

$$\sigma_{yx} = \Delta\sigma \sin \beta \cos \beta, \quad (35)$$

where $\Delta\sigma$ has been defined after Eq. (33). The angular dependence of PHC is shown in Fig. 6(a). The PHC reaches the maximum value at an odd multiple of $\pi/4$. The amplitude of PHC ($\Delta\sigma$) shows a quadratic dependence on B for any value of β (except for $\beta = 0$ and $\beta = \pi/2$ where it trivially vanishes) as shown in Fig. 6(b). Since its origin is associated with Berry curvature and not the Lorentz force, the PHC obeys a symmetric relation $\sigma_{yx} = \sigma_{xy}$ unlike the regular Hall conductivity. The other diagonal elements of conductivity

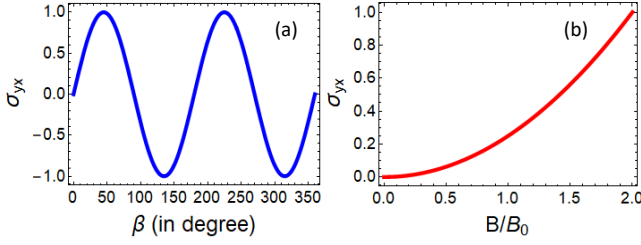


FIG. 6: (a) Plot of the angular behavior of planar Hall conductivity σ_{yx} (normalized by $\sigma_{yx}(\beta = \pi/4)$) at $B/B_0 = 2$ for the quadratic TCFs with two triple-component nodes. PHC follows the standard angular trend of $\sin \beta \cos \beta$. (b) The amplitude of PHC (normalised by its amplitude for $B/B_0 = 2$) as a function of magnetic field. PHC shows B^2 dependence on the magnetic field. We have taken $\mu/\mu_0 = 10$.

for different directions of electric field are calculated as: $\sigma_{yy}(\beta) = \sigma_{xx}(\pi/2 - \beta)$ and the zz -component of conductivity is given by

$$\sigma_{zz} = e^2\tau \int \frac{d^3k}{(2\pi)^3} (D_{\mathbf{k}}^{-1}) v_z^2 \left(-\frac{\partial f_{\text{eq}}}{\partial \epsilon_{\mathbf{k}}} \right), \quad (36)$$

It also follows quadratic- B dependence as shown in Fig. 5(d) and no angular dependence. It is to be noted that the lowest-order magnetic field correction to the conductivity comes quadratic and the B -linear dependence of conductivity is zero in our system. All the other off-diagonal components of conductivity are calculated to be zero.

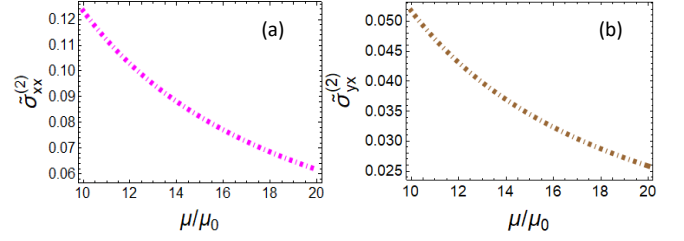


FIG. 7: (a)-(b) depicts the behavior of quadratic B -correction to longitudinal magnetoconductivity (at $\beta = 0$) and planar Hall conductivity (at $\beta = \pi/4$) with the Fermi energy at $B/B_0 = 2$. The quadratic in B component of LMC and PHC shows decrease with the Fermi energy.

Dependence on the Fermi energy (μ/μ_0): In Fig. 7(a) and 7(b), the variation of quadratic in B component of the longitudinal magnetoconductivity ($\sigma_{xx}^{(2)}$) and planar Hall conductivity ($\sigma_{yx}^{(2)}$) is plotted with respect to the Fermi energy. Both of them decrease with the Fermi energy. This is expected because the magnitude of Berry curvature decreases as the Fermi energy shifts away from the band touching node.

B. Magnetic field applied in the x - z plane

Now, we consider another planar Hall setup where the electric field is applied along the z direction ($\mathbf{E} = E\hat{z}$) and the magnetic field is rotated in the x - z plane such that it makes an angle β with respect to the z axis, i.e., $\mathbf{B} = (B \sin \beta, 0, B \cos \beta)$.

The longitudinal magnetoconductivity for the above configuration using Eq. (21) can be written as

$$\sigma_{zz} = e^2\tau \int \frac{d^3k}{(2\pi)^3} D_{\mathbf{k}}^{-1} \left[v_z + \frac{eB \cos \beta}{\hbar} (\mathbf{v}_{\mathbf{k}} \cdot \boldsymbol{\Omega}_{\mathbf{k}}) \right]^2 \left(-\frac{\partial f_{\text{eq}}}{\partial \epsilon_{\mathbf{k}}} \right). \quad (37)$$

The above expression takes the following form

$$\sigma_{zz} = \sigma_{zz}^{(0)} + \sigma_1 + \sigma_2 \cos^2 \beta, \quad (38)$$

where $\sigma_{zz}^{(0)}$ is the Drude conductivity given by Eq. (31) and the conductivity coefficients σ_1 and σ_2 are proportional to B^2 . All the three terms of σ_{zz} show significant dependence on Fermi energy. The longitudinal magnetoconductivity shows the angular dependence of $\cos^2 \beta$ as shown in Fig. 8(a). Its B^2 dependence (except at $\beta = \pi/2$) is depicted in Fig. 8(b). The simplified expression of the planar Hall conductivity for B applied in the x - z plane can be written as

$$\sigma_{zx} = e^2\tau \int \frac{d^3k}{(2\pi)^3} (D_{\mathbf{k}})^{-1} \left[v_z + \frac{eB \cos \beta}{\hbar} (\mathbf{v}_{\mathbf{k}} \cdot \boldsymbol{\Omega}_{\mathbf{k}}) \right] \left[v_x + \frac{eB \sin \beta}{\hbar} (\mathbf{v}_{\mathbf{k}} \cdot \boldsymbol{\Omega}_{\mathbf{k}}) \right] \left(-\frac{\partial f_{\text{eq}}}{\partial \epsilon_{\mathbf{k}}} \right), \quad (39)$$

We can also write the PHC as

$$\sigma_{zx} = \sigma_3 \sin \beta \cos \beta. \quad (40)$$

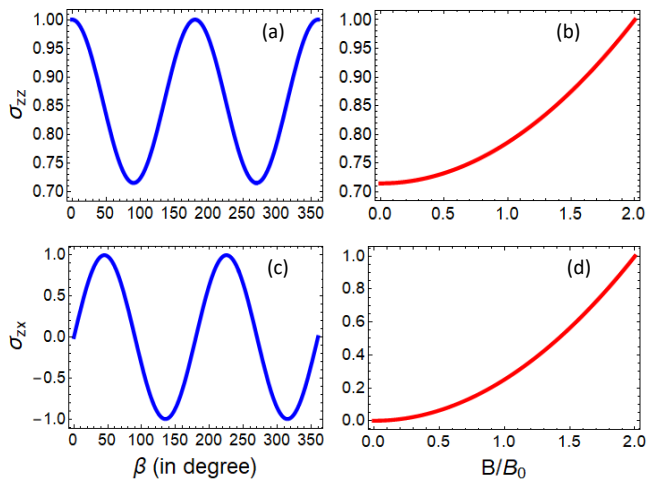


FIG. 8: (a) and (c) shows the angular dependence of longitudinal magnetoconductivity ($\sigma_{zz} \propto \cos^2 \beta$) and planar Hall conductivity ($\sigma_{zx} \propto \sin \beta \cos \beta$) calculated numerically for the quadratic TCFs, when a magnetic field is rotated in the x - z plane at $B/B_0 = 2$. Here, the y axes of (a) and (c) are normalized by $\sigma_{zz}(\beta = 0)$ and $\sigma_{zx}(\beta = \pi/4)$ respectively. (b) and (d) depicts the variation of LMC at $\beta = 0$ (normalized by σ_{zz} for $B/B_0 = 2$) and the amplitude of planar Hall conductivity (normalized by σ_{zx} for $B/B_0 = 2$) as a function of magnetic field. The calculations are performed at $\mu/\mu_0 = 10$.

Its angular and quadratic- B dependences are shown in Fig. 8(c) and Fig. 8(d) respectively. The maximum value is obtained at $\beta = \pi/4$. The variations of quadratic in B component of the longitudinal magnetoconductivity ($\sigma_{zz}^{(2)}$) and planar Hall conductivity (σ_{zx}) with respect to the Fermi energy are plotted in Fig. 9(a). Similar to the previous orientation, both the quantities decrease with Fermi energy.

The other diagonal components of the conductivity are obtained as

$$\sigma_{xx} = \sigma_{xx}^{(0)} + \sigma_4 \cos^2 \beta + \sigma_5 \sin^2 \beta \quad (41)$$

and

$$\sigma_{yy} = \sigma_{yy}^{(0)} + \sigma_4 \cos^2 \beta + \sigma_6 \sin^2 \beta. \quad (42)$$

Here, $\sigma_{xx}^{(0)} = \sigma_{yy}^{(0)}$, calculated numerically from Eq. (30). Apart from the Drude parts, there are quadratic- B corrections in conductivity viz. σ_4 , σ_5 and σ_6 . Here, σ_4 denotes the quadratic- B correction in both σ_{xx} and σ_{yy} when $\mathbf{B} \parallel \hat{\mathbf{z}}$ while σ_5 and σ_6 denotes the quadratic- B correction in σ_{xx} and σ_{yy} respectively when $\mathbf{B} \parallel \hat{\mathbf{x}}$. The variation of these correction terms with Fermi energy is shown in Fig. 9(b). We observe that σ_4 is independent of Fermi energy while σ_5 and σ_6 show a decrease.

An important feature which distinguishes this orientation of planar Hall geometry from the previous one is that the out-of-plane component of conductivity σ_{yy} also has an oscillatory behaviour as the magnetic field is rotated in the x - z plane.

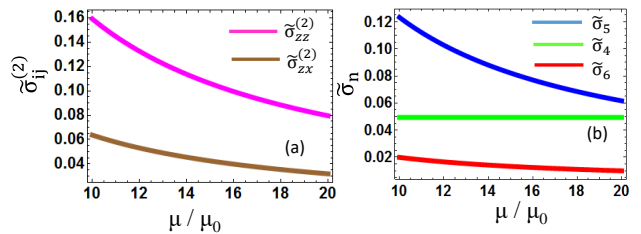


FIG. 9: (a) Plots of variation of quadratic B -correction to longitudinal magnetoconductivity ($\sigma_{zz}^{(2)}$ at $\beta = 0$) and planar Hall conductivity ($\sigma_{zx}^{(2)}$ at $\beta = \pi/4$) with the Fermi energy for $B/B_0 = 2$ respectively. In both the cases, the quadratic in B component of LMC and PHC shows decrease with the Fermi energy. (b) Dependence of the quadratic- B correction in σ_{xx} and σ_{yy} when $\mathbf{B} \parallel \hat{\mathbf{x}}$, i.e., (σ_5 and σ_6) with the Fermi energy. Both the conductivity coefficients decrease with the Fermi energy. The quadratic- B correction in both σ_{xx} and σ_{yy} when $\mathbf{B} \parallel \hat{\mathbf{z}}$ denoted by σ_4 is independent of the Fermi energy. In the plot, σ_4 is divided by a factor of 10.

V. MAGNETORESISTANCE

We have evaluated the magnetoconductivity matrix numerically from the low-energy model of the quadratic TCFs for two different planar geometries in the last section. Next, we calculate the magnetoresistance which is defined as

$$\text{MR}_{ii} = \frac{\rho_{ii}(B) - \rho_{ii}(0)}{\rho_{ii}(0)}, \quad (43)$$

where ρ_{ii} denotes the diagonal components of the resistivity tensor with $i = x, y, z$. The Drude resistivity $\rho_{ii}(0)$ is simply the inverse of Drude conductivity $\sigma_{ii}^{(0)}$. In this section also, we study and compare magnetoresistance for the two orientations of magnetic field mentioned earlier.

For the case of magnetic field applied in the x - y plane making an angle β with the x axis, the planar MR [$\text{MR}_{xx}(\beta)$] is anisotropic as it shows an angular variation of $\cos^2 \beta$ shown in Fig. 10(a). The decrease in magnetoresistivity is maximum at $\beta = 0$ and π and minimum at $\beta = \pi/2$. It is evident from Fig. 10(a), when $\mu/\mu_0 = 10$ and $B/B_0 = 2$, the negative MR resulting from the Berry curvature is about -1.8% at $\beta = 0$ and π . We have plotted the magnetic field dependence of longitudinal MR (MR_{xx}) at $\beta = 0$ in Fig. 10(b). For the second orientation where applied magnetic field is rotated in the x - z plane by making an angle β with the z axis, the planar MR is denoted by [$\text{MR}_{zz}(\beta)$] which also follows the angular dependence of $\cos^2 \beta$ as shown in Fig. 10(c). Here, the MR reaches about -29% and thus the Berry curvature effects on MR are considerably large in this orientation. The increasing nature of absolute longitudinal MR (MR_{zz}) at $\beta = 0$ with the magnetic field is shown in Fig. 10(d).

Dependence on the Fermi energy (μ/μ_0): The longitudinal magnetoresistances MR_{xx} and MR_{zz} corresponding to their respective magnetic field configurations

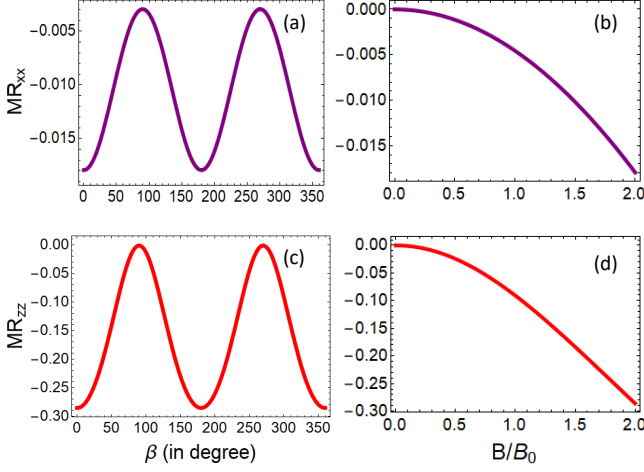


FIG. 10: The angular and magnetic field dependence of magnetoresistance for quadratic TCFs evaluated for two different configurations of the magnetic field. Here, the purple curve represents the case of magnetic field applied in the x - y plane whereas red curve denotes the magnetic field confined in the x - z plane. The planar MR [$MR_{xx}(\beta)$] and [$MR_{zz}(\beta)$] varies as $\cos^2 \beta$ corresponding to their respective magnetic field configuration at $B/B_0 = 2$ is shown in (a) and (c). The variation of longitudinal magnetoresistance: (b) MR_{xx} and (d) MR_{zz} as a function of magnetic field at $\beta = 0$. We have used $\mu/\mu_0 = 10$.

are plotted as function of Fermi energy in Fig. 11(a) and 11(b). The absolute value of MR in both the cases decrease with the Fermi energy.

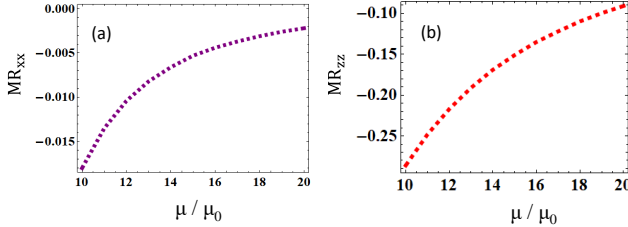


FIG. 11: The variation of magnetoresistance with the Fermi energy. (a) The longitudinal MR (MR_{xx}) corresponds to the case of magnetic field applied in the x - y plane (purple dashed curve) and (b) MR_{zz} is the longitudinal MR for the magnetic field confined in the x - z plane (red dashed curve). In both the cases, the absolute value of MR decreases with the Fermi energy. We have used the following parameters: $B/B_0 = 2$ and $\beta = 0$.

VI. THERMAL CONDUCTIVITY

The thermal current is defined as^{53,59}

$$\mathbf{j}_q = \int [d\mathbf{k}] D_{\mathbf{k}} (\epsilon_{\mathbf{k}} - \mu) \dot{\mathbf{r}}_{\mathbf{k}}, \quad (44)$$

Substituting $\dot{\mathbf{r}}$ and $f_{\mathbf{k}}$ from Eqs. (15) and (17) in Eq. (44) yields the following general expression of Berry curvature dependent thermal conductivity:

$$\begin{aligned} \kappa_{ij} = & -\frac{1}{\hbar} \int [d\mathbf{k}] \epsilon_{ijl} \Omega_{\mathbf{k}}^l \frac{(\epsilon_{\mathbf{k}} - \mu)^2}{T} f_{\text{eq}} \\ & + \tau \int [d\mathbf{k}] (D_{\mathbf{k}})^{-1} \left(v_i + \frac{e}{\hbar} B_i (\mathbf{v}_{\mathbf{k}} \cdot \boldsymbol{\Omega}_{\mathbf{k}}) \right) \\ & \left(v_j + \frac{e}{\hbar} B_j (\mathbf{v}_{\mathbf{k}} \cdot \boldsymbol{\Omega}_{\mathbf{k}}) \right) \frac{(\epsilon_{\mathbf{k}} - \mu)^2}{T} \left(-\frac{\partial f_{\text{eq}}}{\partial \epsilon_{\mathbf{k}}} \right), \end{aligned} \quad (45)$$

where the first term corresponds to the anomalous thermal Hall conductivity without magnetic field. The longitudinal thermal conductivity in the absence of magnetic field is obtained as

$$\kappa_{ii}^{(0)} = \tau \int \frac{d^3k}{(2\pi)^3} v_i^2 \frac{(\epsilon_{\mathbf{k}} - \mu)^2}{T} \left(-\frac{\partial f_{\text{eq}}}{\partial \epsilon_{\mathbf{k}}} \right). \quad (46)$$

A. Magnetic field is applied in the x - y plane

We will now investigate the longitudinal magneto-thermal conductivity and planar thermal Hall conductivity for a configuration where temperature gradient is applied along the x axis and magnetic field is in the x - y plane making an angle β from the x axis such that $\nabla T = \nabla T \hat{x}$, $\mathbf{B} = (B \cos \beta, B \sin \beta, 0)$ and $\mathbf{E} = 0$.

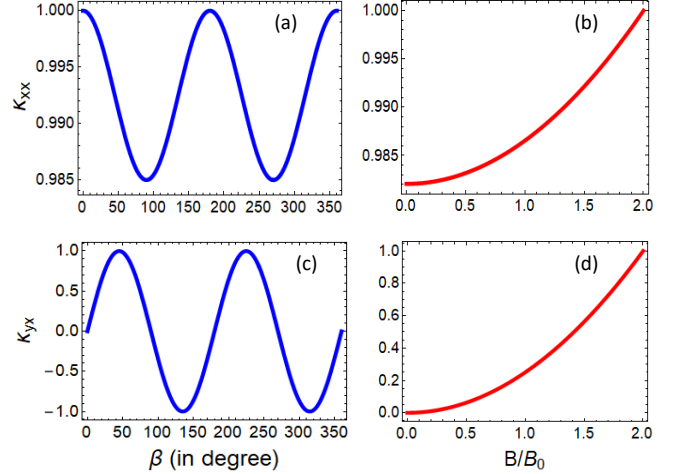


FIG. 12: (a) The angular dependence of longitudinal magneto-thermal conductivity κ_{xx} (normalized by $\kappa_{xx}(\beta = 0)$) computed numerically for the quadratic TCFs at $B/B_0 = 2$. (b) depicts the variation of LMTC at $\beta = 0$ (normalized by κ_{xx} for $B/B_0 = 2$) as a function of magnetic field. (c) shows the plot of the angular behavior of planar thermal Hall conductivity κ_{yx} at $B/B_0 = 2$. (d) The amplitude of PTHC shows the quadratic- B dependence. Here, the y axes of (c) and (d) are normalized by $\kappa_{yx}(\beta = \pi/4)$ and $\kappa_{yx}(B/B_0 = 2)$ respectively. The calculations are performed at $\mu/\mu_0 = 10$ and $T = 300$ K.

Next, we consider the temperature gradient and magnetic field are parallel in order to calculate the longitudinal magneto-thermal conductivity which is given by the

following expression as

$$\kappa_{xx} = \tau \int [d\mathbf{k}] \frac{(\epsilon_{\mathbf{k}} - \mu)^2}{(D_{\mathbf{k}})T} \left[v_x + \frac{eB \cos \beta}{\hbar} (\mathbf{v}_{\mathbf{k}} \cdot \boldsymbol{\Omega}_{\mathbf{k}}) \right]^2 \left(-\frac{\partial f_{\text{eq}}}{\partial \epsilon_{\mathbf{k}}} \right). \quad (47)$$

We can further express the magneto-thermal conductivity in the planar configuration κ_{xx} in terms of κ_{\parallel} and κ_{\perp} describing the cases of thermal current flowing parallel and perpendicular to the magnetic field as

$$\kappa_{xx} = \kappa_{\perp} + \Delta\kappa \cos^2 \beta. \quad (48)$$

Here $\Delta\kappa = \kappa_{\parallel} - \kappa_{\perp}$ with $\kappa_{\parallel} = \kappa_{xx}(\beta = 0) = \kappa_{xx}^{(0)} + \kappa_{\parallel}^{(2)}$ and $\kappa_{\perp} = \kappa_{xx}(\beta = \pi/2) = \kappa_{xx}^{(0)} + \kappa_{\perp}^{(2)}$. The longitudinal magneto-thermal conductivity has the angular dependence of $\cos^2 \beta$ which is depicted in Fig. 12(a) and thus shows anisotropic behavior. The LMTC shows the quadratic- B dependence on the magnetic field (except at $\beta = \pi/2$) for the quadratic TCFs at $T = 300$ K as shown in Fig. 12(b).

Planar thermal Hall effect: The PTHC⁵⁵ is defined as the appearance of in-plane transverse temperature gradient when the applied temperature gradient and magnetic field are coplanar. It is the thermal analog of planar Hall effect. The expression for planar thermal Hall conductivity is obtained as

$$\kappa_{yx} = \tau \int \frac{d^3k}{(2\pi)^3} \frac{(\epsilon_{\mathbf{k}} - \mu)^2}{(D_{\mathbf{k}})T} \left[v_x + \frac{eB \cos \beta}{\hbar} (\mathbf{v}_{\mathbf{k}} \cdot \boldsymbol{\Omega}_{\mathbf{k}}) \right] \left[v_y + \frac{eB \sin \beta}{\hbar} (\mathbf{v}_{\mathbf{k}} \cdot \boldsymbol{\Omega}_{\mathbf{k}}) \right] \left(-\frac{\partial f_{\text{eq}}}{\partial \epsilon_{\mathbf{k}}} \right), \quad (49)$$

The PHTC can be further expressed as

$$\kappa_{yx} = \Delta\kappa \sin \beta \cos \beta. \quad (50)$$

The planar thermal Hall conductivity follows the angular dependence of $\sin \beta \cos \beta$. The amplitude of PTHC ($\Delta\kappa$) shows a B^2 dependence for any value of β except for $\beta = 0$ and $\beta = \pi/2$. We have plotted the angular and magnetic field dependence of κ_{yx} at $T = 300$ K in Fig. 12(c) and 12(d) respectively.

B. Magnetic field is applied in the x - z plane

Next, we fix the direction of temperature gradient along the z axis and magnetic field is rotated in the x - z plane making an angle β from the z axis and thus we have $\nabla T = \nabla T \hat{z}$, $\mathbf{B} = (B \sin \beta, 0, B \cos \beta)$, and $\mathbf{E} = 0$. We have evaluated the longitudinal magneto-thermal conductivity κ_{zz} and planar thermal Hall conductivity κ_{zx} and discuss the numerical results of the above thermal conductivities. The longitudinal magneto-thermal conductivity for this configuration can be expressed as

$$\kappa_{zz} = \kappa_{zz}^{(0)} + \kappa_1 + \kappa_2 \cos^2 \beta. \quad (51)$$

The planar thermal Hall conductivity is given by

$$\kappa_{zx} = \kappa_3 \sin \beta \cos \beta. \quad (52)$$

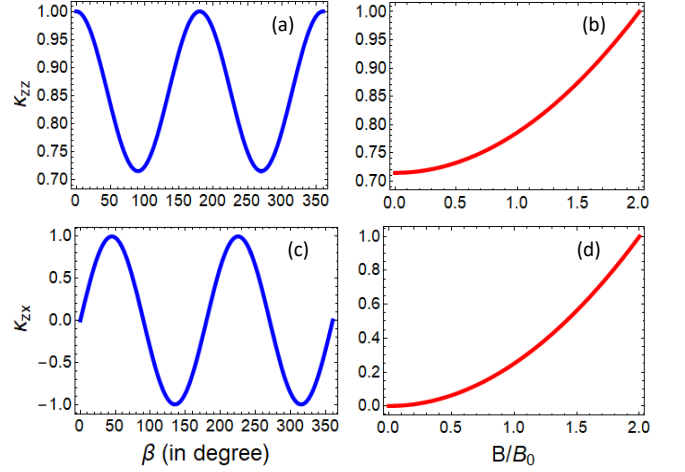


FIG. 13: (a) and (c) depicts the angular dependence of longitudinal magneto-thermal conductivity ($\kappa_{zz} \propto \cos^2 \beta$) and planar thermal Hall conductivity ($\kappa_{zx} \propto \sin \beta \cos \beta$) for the quadratic TCFs, when a magnetic field is rotated in the x - z plane at $B/B_0 = 2$. Here, the y axes of (a) and (c) are normalized by $\kappa_{zz}(\beta = 0)$ and $\kappa_{zx}(\beta = \pi/4)$ respectively. (b) and (d) The variation of LMTC at $\beta = 0$ (normalized by κ_{zz} for $B/B_0 = 2$) and the amplitude of planar thermal Hall conductivity (normalized by κ_{zx} for $B/B_0 = 2$) as a function of magnetic field. We have used the parameter: $\mu/\mu_0 = 10$ and $T = 300$ K.

Here, the thermal conductivity coefficients (κ_1, κ_2 and κ_3) are proportional to B^2 . The longitudinal magneto-thermal conductivity κ_{zz} has the angular dependence of $\cos^2 \beta$ as depicted in Fig. 13(a), whereas the planar thermal Hall conductivity follows the standard $\sin \beta \cos \beta$ dependence which is shown in Fig. 13(c). Fig. 13(b) and 13(d) depicts the variation of κ_{zz} and κ_{zx} with the magnetic field for the quadratic TCFs at $T = 300$ K. Both the LMTC and PTHC shows quadratic dependence on the magnetic field.

Validity of Wiedemann-Franz law: The Wiedemann-Franz law states that the ratio of electronic contribution of thermal conductivity to electrical conductivity for metal is proportional to the temperature and can be expressed as $\kappa_{ij}/(\sigma_{ij}T) = L_0$, where $L_0 = \frac{\pi^2 K_B^2}{3e^2}$ is the Lorentz number. The Wiedemann-Franz law is valid in our case of TRS broken quadratic TCFs for the numerically computed electrical and thermal conductivities at $T = 300$ K.

VII. QUANTITATIVE COMPARISON OF THE TRANSPORT COEFFICIENTS

In this section, we compare the magnitudes of transport coefficients for the two orientations by plotting their ratios with respect to magnetic field and Fermi energy. In Fig. 14(a), the ratio of longitudinal magnetoconductivities σ_{zz} and σ_{xx} of the respective orientations is plotted

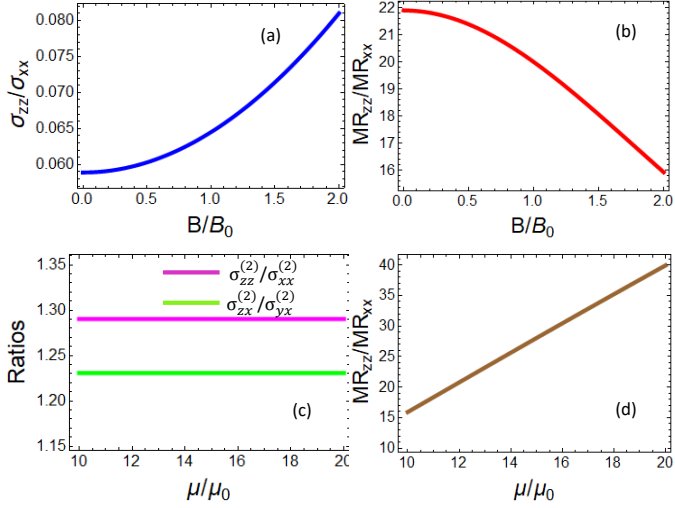


FIG. 14: Plots of (a) the ratio of longitudinal magnetoconductivities (σ_{zz}/σ_{xx}) and (b) ratio of longitudinal MR ($\text{MR}_{zz}/\text{MR}_{xx}$) of the respective orientations as a function of B for $\mathbf{E} \parallel \mathbf{B}$. (c) Ratio of quadratic- B correction to longitudinal magnetoconductivities ($\sigma_{zz}^{(2)}/\sigma_{xx}^{(2)}$) and planar Hall conductivities ($\sigma_{zx}^{(2)}/\sigma_{yx}^{(2)}$) for the two orientation are independent of Fermi energy. (d) The ratio of longitudinal MR ($\text{MR}_{zz}/\text{MR}_{xx}$) as a function of Fermi energy.

as a function of B for $\mathbf{E} \parallel \mathbf{B}$. As $B \rightarrow 0$, the ratio refers to that of the Drude conductivities. The value of $\sigma_{zz}^{(0)}$ is $\sim 6\%$ of that $\sigma_{xx}^{(0)}$ for the chosen set of parameters, which implies a highly reduced Drude conductivity along z axis. The ratio σ_{zz}/σ_{xx} is a slowly increasing function of B . The increase is only $\sim 2\%$ upto $B/B_0 = 2$. Figure 14(b) shows that the ratio of the magnetoresistances is a decreasing function of B . At very low B , MR_{zz} is nearly 22 times of MR_{xx} . The ratio drops to ~ 16 at $B/B_0 = 2$. Thus, the direction in which the energy scales linearly with momentum in quadratic TCFs favours higher magnitude of MR and lower value of longitudinal magnetoconductivity. The measurements of MR and resistivity in presence of small magnetic field may hence act as probes for detecting different symmetry axes of the system.

We also observe that the ratio of quadratic- B correction to longitudinal magnetoconductivities ($\sigma_{zz}^{(2)}/\sigma_{xx}^{(2)}$) and planar Hall conductivities ($\sigma_{zx}^{(2)}/\sigma_{yx}^{(2)}$) for the two orientations are independent of Fermi energy as shown in Fig. 14(c). The ratio ($\sigma_{zz}^{(2)}/\sigma_{xx}^{(2)}$) is higher than ($\sigma_{zx}^{(2)}/\sigma_{yx}^{(2)}$). The ratio of longitudinal MR ($\text{MR}_{zz}/\text{MR}_{xx}$) is almost a linearly increasing function of Fermi energy as depicted in Fig. 14(d).

The ratio of the thermal coefficients show similar behaviour as that of the electrical ones since the longitudinal thermal and planar thermal Hall conductivities differ from their electrical counterparts simply by a factor (L_0T) within the Sommerfeld approximation.

VIII. CONCLUSIONS

Triple-component semimetals host crossings of three energy bands near which the quasiparticles behave like pseudospin-1 fermions. In this work, we have dealt with the low-energy model for generalized triple-component fermions and obtained the Berry curvature, density of states and Fermi energy as function of carrier density. The DOS of dispersive bands varies with the Fermi energy as $D_n(\mu) \sim \mu^{2/n}$, where $n = 1, 2, 3$. The Fermi energy as a function of electron density scales as $\mu \sim n_e^{n/n+2}$. These exponents are independent of the coefficients ν_z and α_n .

We have specifically considered quadratic TCFs i.e., $n = 2$ case and studied its Berry curvature induced electrical and thermal magnetotransport properties using semiclassical Boltzmann transport formalism. On the account of anisotropic energy spectrum of quadratic TCFs, we have obtained the transport coefficients for two different orientations of magnetic field – \mathbf{B} applied in x - y and x - z plane. Planar Hall effect is observed in both the orientations due to Berry curvature-modified magnetotransport. The PHC shows B^2 dependence in the lowest order in B and an angular dependence of $\sin \beta \cos \beta$ as observed in other topological semimetals, where β is the angle between applied electric and magnetic fields. The longitudinal magnetoconductivity also follows B^2 dependence due to Berry curvature, resulting in negative longitudinal MR. The longitudinal magnetoresistances corresponding to their respective B -field configurations ($\text{MR}_{xx}(\beta)$ and $\text{MR}_{zz}(\beta)$) vary as $\cos^2 \beta$. We find that the out-of-plane magnetoconductivity shows an oscillatory dependence with β for the second orientation of magnetic field, but it is angle-independent for the first one.

For the case of B applied in x - y plane, negative MR has the maximum value of about -1.8% whereas for B confined in x - z plane, the maximum MR reaches about -29% . Hence it is evident that Berry curvature effects are considerably large for the latter case. Thus, the direction in which the energy scales linearly with momentum in quadratic TCFs favours higher magnitude of longitudinal MR.

The Drude conductivities $\sigma_{xx}^{(0)}$ and $\sigma_{zz}^{(0)}$ are increasing functions of Fermi energy. The second-order corrections in longitudinal and planar magnetoconductivities and the absolute MRs for both the orientations decrease with the Fermi energy. This is attributed to the fact that Berry curvature effects decrease as the Fermi energy moves away from the band-touching nodes. The ratio ($\text{MR}_{zz}/\text{MR}_{xx}$) is almost a linearly increasing function of Fermi energy. A noteworthy feature of quadratic triple-component fermions which is typically absent in conventional systems is that certain transport coefficients and their ratios are independent of Fermi energy within the low-energy model. We observed that when B is applied in the x - z plane, quadratic B -correction in both σ_{xx} and σ_{yy} for $\mathbf{B} \parallel \hat{\mathbf{z}}$ is independent of Fermi energy. Further-

more, the ratio of quadratic- B correction to longitudinal magnetoconductivities ($\sigma_{zz}^{(2)}/\sigma_{xx}^{(2)}$) and planar Hall conductivities ($\sigma_{zx}^{(2)}/\sigma_{yx}^{(2)}$) corresponding to their respective orientations are also independent of Fermi energy.

We also studied the longitudinal magneto-thermal conductivity and planar thermal Hall conductivity in quadratic TCFs for both the magnetic field configurations. We note that LMTC and PTHC show similar angular dependences as those of LMC and PHC and follow quadratic- B dependence. Additionally, we find that Wiedemann-Franz law is valid for the numerically computed electrical and thermal conductivities at $T = 300$ K.

It is to be noted that in inversion symmetry broken and TRS preserved TCFs, the band touching nodes should appear in multiple of 4 just like the case of inversion symmetry broken Weyl semimetals. So, the magnitudes

of the magnetotransport coefficients will be enhanced due to contribution from a greater number of nodes. Also, in such systems the triple-component nodes may not be at the same energy. This may result in different values of density of states, velocities and Berry curvatures at the Fermi surface of different nodes, unlike the TRS broken case. Moreover, in such systems, it is possible that the Fermi surface may intersect conduction band near one node (electron-like) and valence-band near the other (hole-like). So, we have to calculate the total magnetotransport coefficients considering low-energy Hamiltonians around each node separately.

ACKNOWLEDGEMENTS

We would like to thank Sonu Verma for useful discussions.

Appendix A: Lorentz-force contribution

The components of $\mathbf{\Gamma}_m$ in Eq. (17) for electrical and thermal transport are given below^{48,55}. For brevity, we have dropped the band index m .

(a). For the planar Hall setup: $\mathbf{E} = E\hat{x}$, $\mathbf{B} = (B \cos \beta, B \sin \beta, 0)$ and $\nabla T = 0$,

$$\Gamma_z = \frac{N(M_1M_2 + M_3M_4)}{\left(\frac{D}{\tau}\right)^2 - \left(\frac{eB \cos \beta}{m_{yz}} - \frac{eB \sin \beta}{m_{xz}}\right)^2 - \frac{eB}{m_{zz}}M_4}, \quad (\text{A1})$$

$$\Gamma_y = -\frac{\cos \beta [NM_3 + \Gamma_z \frac{eB}{m_{zz}}]}{M_2}, \quad \Gamma_x = -\tan \beta \Gamma_y, \quad (\text{A2})$$

where $m_{ij} = \frac{1}{\hbar^2} \frac{\partial^2 \epsilon_{\mathbf{k}}}{\partial k_i \partial k_j}$ is band-mass tensor, $N = \frac{e^2 EB \tau}{D}$, $M_1 = -\frac{\sin \beta}{m_{xx}} + \frac{\cos \beta}{m_{xy}} + \frac{eB \cos \beta}{\hbar} (C_2 \cos \beta - C_1 \sin \beta)$, $M_2 = \frac{D}{\tau} - \frac{eB \sin \beta}{m_{xz}} + \frac{eB \cos \beta}{m_{yz}}$, $M_3 = \frac{eB \cos \beta}{\hbar} C_3 + \frac{1}{m_{xz}}$, $M_4 = \frac{eB \sin 2\beta}{m_{xy}} - \frac{eB \cos^2 \beta}{m_{yy}} - \frac{eB \sin^2 \beta}{m_{xx}}$, $C_1 = \frac{\Omega_x}{m_{xx}} + \frac{\Omega_y}{m_{xy}} + \frac{\Omega_z}{m_{xz}}$, $C_2 = \frac{\Omega_x}{m_{xy}} + \frac{\Omega_y}{m_{yy}} + \frac{\Omega_z}{m_{yz}}$ and $C_3 = \frac{\Omega_x}{m_{xz}} + \frac{\Omega_y}{m_{yz}} + \frac{\Omega_z}{m_{zz}}$.

(b). For the planar Hall setup: $\mathbf{B} = (B \cos \beta, B \sin \beta, 0)$, $\nabla T = \nabla T \hat{x}$ and $\mathbf{E} = 0$,

$$\Gamma_z = \frac{N_0(\alpha_1 \alpha_2 - \alpha_3 \alpha_4)}{\left(\frac{D}{\tau}\right)^2 - \left(\frac{eB \cos \beta}{m_{yz}} - \frac{eB \sin \beta}{m_{xz}}\right)^2 - \frac{eB}{m_{zz}} \alpha_4}, \quad (\text{A3})$$

$$\Gamma_y = \frac{\cos \beta [N_0 \left(\frac{1}{m_{xz}} + \frac{eB C_3 \cos \beta}{\hbar}\right) - \Gamma_z \frac{eB}{m_{zz}}]}{\left(\frac{eB \cos \beta}{m_{yz}} - \frac{D}{\tau} - \frac{eB \sin \beta}{m_{xz}}\right)}, \quad (\text{A4})$$

$$\Gamma_x = -\tan \beta \Gamma_y, \quad (\text{A5})$$

where $N_0 = eB\tau \nabla T \frac{(\epsilon_{\mathbf{k}} - \mu)}{DT}$, $\alpha_1 = \frac{\sin \beta}{m_{xx}} - \frac{\cos \beta}{m_{xy}} + \frac{eB \cos \beta}{\hbar} (-C_2 \cos \beta + C_1 \sin \beta)$, $\alpha_2 = -\frac{D}{\tau} + \frac{eB \cos \beta}{m_{yz}} - \frac{eB \sin \beta}{m_{xz}}$, $\alpha_3 = \frac{eB \cos \beta}{\hbar} C_3 + \frac{1}{m_{xz}}$, $\alpha_4 = \frac{eB \sin 2\beta}{m_{xy}} - \frac{eB \cos^2 \beta}{m_{yy}} - \frac{eB \sin^2 \beta}{m_{xx}}$.

-
- ¹ S. M. Young, S. Zaheer, J. C. Teo, C. L. Kane, E. J. Mele, and A. M. Rappe, *Phys. Rev. Lett.* **108**, 140405 (2012).
- ² Z. Wang, Y. Sun, X.-Q. Chen, C. Franchini, G. Xu, H. Weng, X. Dai, and Z. Fang, *Phys. Rev. B* **85**, 195320 (2012).
- ³ Z. K. Liu, B. Zhou, Y. Zhang, Z. J. Wang, H. M. Weng, D. Prabhakaran, S.-K. Mo, Z. X. Shen, Z. Fang, X. Dai, Z. Hussain, Y. L. Chen, *Science* **343**, 864 (2014).
- ⁴ Z. Liu, J. Jiang, B. Zhou, Z. Wang, Y. Zhang, H. Weng, D. Prabhakaran, S. Mo, H. Peng, P. Dudin, T. Kim, M. Hoesch, Z. Fang, X. Dai, Z. X. Shen, D. L. Feng, Z. Hussain, Y. L. Chen, *Nat. Mater.* **13**, 677 (2014).
- ⁵ J. Xiong, S. K. Kushwaha, T. Liang, J. W. Krizan, M. Hirschberger, W. Wang, R. J. Cava, and N. P. Ong, *Science* **350**, 413 (2015).
- ⁶ X. Wan, A. M. Turner, A. Vishwanath, and S. Y. Savrasov, *Phys. Rev. B* **83**, 205101 (2011).
- ⁷ H. Weng, C. Fang, Z. Fang, B. A. Bernevig, and X. Dai, *Phys. Rev. X* **5**, 011029 (2015).
- ⁸ S. M. Huang, S. Y. Xu, I. Belopolski, C. C. Lee, G. Chang, B. K. Wang, N. Alidoust, G. Bian, M. Neupane, C. Zhang, S. Jia, A. Bansil, H. Lin, and M. Z. Hasan, *Nat. Comm.* **6**, 7373 (2015).
- ⁹ S.-Y. Xu, N. Alidoust, I. Belopolski, Z. Yuan, G. Bian, T.-R. Chang, H. Zheng, V. N. Strocov, D. S. Sanchez, G. Chang, C. Zhang, D. Mou, Y. Wu, L. Huang, C.-C. Lee, S.-M. Huang, B. Wang, A. Bansil, H.-T. Jeng, T. Neupert, A. Kaminski, H. Lin, S. Jia and M. Z. Hasan, *Nat. Phys.* **11**, 748 (2015).
- ¹⁰ B. Q. Lv, H. M. Weng, B. B. Fu, X. P. Wang, H. Miao, J. Ma, P. Richard, X. C. Huang, L. X. Zhao, G. F. Chen, Z. Fang, X. Dai, T. Qian, and H. Ding, *Phys. Rev. X* **5**, 031013 (2015).
- ¹¹ B. Q. Lv, N. Xu, H. M. Weng, J. Z. Ma, P. Richard, X. C. Huang, L. X. Zhao, G. F. Chen, C. E. Matt, F. Bisti, V. N. Strocov, J. Mesot, Z. Fang, X. Dai, T. Qian, M. Shi, and H. Ding, *Nat. Phys.* **11**, 724 (2015).
- ¹² S.-Y. Xu, I. Belopolski, N. Alidoust, M. Neupane, G. Bian, C. Zhang, R. Sankar, G. Chang, Z. Yuan, C.-C. Lee, S.-M. Huang, H. Zheng, J. Ma, D. S. Sanchez, B. Wang, A. Bansil, F. Chou, P. P. Shibayev, H. Lin, S. Jia, and M. Zahid Hasan, *Science* **349**, 613 (2015).
- ¹³ A. A. Soluyanov, D. Gresch, Z. Wang, Q. Wu, M. Troyer, X. Dai, and B. A. Bernevig, *Nature* **527**, 495 (2015).
- ¹⁴ B. Bradlyn, J. Cano, Z. Wang, M. G. Vergniory, C. Felser, R. J. Cava, and B. A. Bernevig, *Science* **353**, 6299 (2016).
- ¹⁵ G. Chang, S.-Y. Xu, S.-M. Huang, D. S. Sanchez, C.-H. Hsu, G. Bian, Z.-M. Yu, I. Belopolski, N. Alidoust, H. Zheng, T.-R. Chang, H.-T. Jeng, S. A. Yang, T. Neupert, H. Lin, and M. Z. Hasan, *Scientific Reports* **7**, 1688 (2017).
- ¹⁶ I. C. Fulga and A. Stern, *Phys. Rev. B* **95**, 241116 (2017).
- ¹⁷ H. Weng, C. Fang, Z. Fang, and X. Dai, *Phys. Rev. B* **94**, 165201 (2016).
- ¹⁸ H. Weng, C. Fang, Z. Fang, and X. Dai, *Phys. Rev. B* **93**, 241202 (2016).
- ¹⁹ C.-H. Cheung, R. C. Xiao, M.-C. Hsu, H.-R. Fuh, Y.-C. Lin, and C.-R. Chang, arXiv:1709.07763.
- ²⁰ J. Li, Q. Xie, S. Ullah, R. Li, H. Ma, D. Li, Y. Li, and X.-Q. Chen, *Phys. Rev. B* **97**, 054305 (2018).
- ²¹ B. Q. Lv, Z.-L. Feng, Q.-N. Xu, X. Gao, J.-Z. Ma, L.-Y. Kong, P. Richard, Y.-B. Huang, V. N. Strocov, C. Fang, H.-M. Weng, Y.-G. Shi, T. Qian, and H. Ding, *Nature (London)* **546**, 627 (2017).
- ²² J. B. He, D. Chen, W. L. Zhu, S. Zhang, L. X. Zhao, Z. A. Ren, and G. F. Chen, *Phys. Rev. B* **95**, 195165 (2017).
- ²³ G. Chang, S.-Y. Xu, B. J. Wieder, D. S. Sanchez, S.-M. Huang, I. Belopolski, T.-R. Chang, S. Zhang, A. Bansil, H. Lin, and M. Z. Hasan, *Phys. Rev. Lett.* **119**, 206401 (2017).
- ²⁴ P. Tang, Q. Zhou, and S.-C. Zhang, *Phys. Rev. Lett.* **119**, 206402 (2017).
- ²⁵ Z. Zhu, G. W. Winkler, Q. S. Wu, J. Li, and A. A. Soluyanov, *Phys. Rev. X* **6**, 031003 (2016).
- ²⁶ S. Nandy, S. Manna, D. Calugaru, and B. Roy, *Phys. Rev. B* **100**, 235201 (2019).
- ²⁷ C. Fang, M. J. Gilbert, X. Dai, and B. A. Bernevig, *Phys. Rev. Lett.* **108**, 266802 (2012).
- ²⁸ M. V. Berry, Quantal phase factors accompanying adiabatic changes, *Proc. R. Soc. London, Ser. A* **392**, 45 (1984).
- ²⁹ D. Xiao, M.-C. Chang, and Q. Niu, *Rev. Mod. Phys.* **82**, 1959 (2010).
- ³⁰ F. D. M. Haldane, *Phys. Rev. Lett.* **93**, 206602 (2004).
- ³¹ T. Jungwirth, Q. Niu, and A. H. MacDonald, *Phys. Rev. Lett.* **88**, 207208 (2002).
- ³² A. A. Burkov, *Phys. Rev. Lett.* **113**, 187202 (2014).
- ³³ A. A. Burkov and L. Balents, *Phys. Rev. Lett.* **107**, 127205 (2011).
- ³⁴ T. Qin, Q. Niu, and J. Shi, *Phys. Rev. Lett.* **107**, 236601 (2011).
- ³⁵ T. Yokoyama and S. Murakami, *Phys. Rev. B* **83**, 161407 (2011).
- ³⁶ P. Goswami and S. Tewari, *Phys. Rev. B* **88**, 245107 (2013).
- ³⁷ H. J. Kim, K. S. Kim, J. F. Wang, M. Sasaki, N. Satoh, A. Ohnishi, M. Kitaura, M. Yang, and L. Li, *Phys. Rev. Lett.* **111**, 246603 (2013).
- ³⁸ K.-S. Kim, H.-J. Kim, and M. Sasaki, *Phys. Rev. B* **89**, 195137 (2014).
- ³⁹ Q. Li, D. E. Kharzeev, C. Zhang, Y. Huang, I. Pletikosic, A. V. Fedorov, R. D. Zhong, J. A. Schneeloch, G. D. Gu, and T. Valla, *Nat. Phys.* **12**, 550 (2016).
- ⁴⁰ X. C. Huang, X. Huang, L. Zhao, Y. Long, P. Wang, D. Chen, Z. Yang, H. Liang, M. Xue, H. Weng, Z. Fang, X. Dai, and G. Chen, *Phys. Rev. X* **5**, 031023 (2015).
- ⁴¹ C. Z. Li, L. X. Wang, H. W. Liu, J. Wang, Z. M. Liao, and D. P. Yu, *Nat. Commun.* **6**, 10137 (2015).
- ⁴² H. Li, H. T. He, H. Z. Lu, H. C. Zhang, H. C. Liu, R. Ma, Z. Y. Fan, S. Q. Shen, and J. N. Wang, *Nat. Commun.* **7**, 10301 (2016).
- ⁴³ C. Zhang, E. Zhang, W. Wang, Y. Liu, Z.-G. Chen, S. Lu, S. Liang, J. Cao, X. Yuan, L. Tang, Q. Li, C. Zhou, T. Gu,

- Y. Wu, J. Zou and F. Xiu, *Nat. Commun.* **8**, 13741 (2017).
- ⁴⁴ F. Arnold, C. Shekhar, S.C. Wu, Y. Sun, R. D. dos Reis, N. Kumar, M. Naumann, M. O. Ajeesh, M. Schmidt, A. G. Grushin, J. H. Bardarson, M. Baenitz, D. Sokolov, H. Borrmann, M. Nicklas, C. Felser, E. Hassinger and B. Yan, *Nat. Commun.* **7**, 11615 (2016).
- ⁴⁵ H. Wang, C.-K. Li, H. Liu, J. Yan, J. Wang, J. Liu, Z. Lin, Y. Li, Y. Wang, L. Li, D. Mandrus, X. C. Xie, J. Feng, and J. Wang, *Phys. Rev. B* **93**, 165127 (2016).
- ⁴⁶ X. Dai, Z. Z. Du, and H.-Z. Lu, *Phys. Rev. Lett.* **119**, 166601 (2017).
- ⁴⁷ O. Pal, B. Dey, and T. K. Ghosh, *J. Phys.: Condens. Matter* **34**, 025702 (2022).
- ⁴⁸ S. Nandy, G. Sharma, A. Taraphder, and S. Tewari, *Phys. Rev. Lett.* **119**, 176804 (2017).
- ⁴⁹ A. A. Burkov, *Phys. Rev. B* **96**, 041110 (2017).
- ⁵⁰ S. Nandy, A. Taraphder, and S. Tewari, *Sci. Rep.* **8**, 14983 (2018).
- ⁵¹ S. Ghosh, D. Sinha, S. Nandy, and A. Taraphder *Phys. Rev. B* **102**, 121105(R) (2020).
- ⁵² G. Sharma, S. Nandy, and S. Tewari *Phys. Rev. B* **102**, 205107 (2020).
- ⁵³ R. Lundgren, P. Laurell, and G. A. Fiete, *Phys. Rev. B* **90**, 165115 (2014).
- ⁵⁴ G. Sharma, P. Goswami, and S. Tewari, *Phys. Rev. B* **93**, 035116 (2016).
- ⁵⁵ S. Nandy, A. Taraphder, and S. Tewari, *Phys. Rev. B* **100**, 115139 (2019).
- ⁵⁶ Tanay Nag and Snehasish Nandy, *J. Phys.: Condens. Matter* **33**, 075504 (2021).
- ⁵⁷ S. Nandy, K. Sengupta, and D. Sen, *Phys. Rev. B* **100**, 085134 (2019).
- ⁵⁸ B. Dey and T. K. Ghosh, arXiv:2109.05195.
- ⁵⁹ N. Ashcroft and N. Mermin, *Solid State Physics*, HRW international editions (Holt, Rinehart and Winston, 1976).
- ⁶⁰ C. Duval, Z. Horvth, P. A. Horvthy, L. Martina, and P. C. Stichel, *Mod. Phys. Lett. B* **20**, 373 (2006).
- ⁶¹ T. Morimoto, S. Zhong, J. Orenstein, and J. E. Moore, *Phys. Rev. B* **94**, 245121 (2016).
- ⁶² D. Xiao, J. Shi, and Q. Niu, *Phys. Rev. Lett.* **95**, 137204 (2005).
- ⁶³ D. T. Son and N. Yamamoto, *Phys. Rev. Lett.*, **109**, 181602 (2012).
- ⁶⁴ A. A. Zyuzin and A. A. Burkov, *Phys. Rev. B* **86**, 115133 (2012).
- ⁶⁵ S. Adler, *Phys. Rev.* **177**, 2426 (1969).
- ⁶⁶ J. S. Bell and R. A. Jackiw, *Nuovo Cimento A* **60**, **47** (1969).
- ⁶⁷ H. B. Nielsen and M. Ninomiya, *Phys. Lett. B* **105**, 219 (1981).